Ratios of $^{15}N/^{12}C$ and $^{4}He/^{12}C$ inclusive electroproduction cross sections in the nucleon resonance region

P.E. Bosted,[35,*] R. Fersch,[39] G. Adams,[31] M. Amarian,[29] S. Anefalos,[17] M. Anghinolfi,[18] G. Asryan,[40] H. Avakian,[17,35] H. Bagdasaryan,[40,29] N. Baillie,[39] J.P. Ball,[2] N.A. Baltzell,[34] S. Barrow,[13] V. Batourine,[35] M. Battaglieri,[18] K. Beard,[21] I. Bedlinskiy,[20] M. Bektasoglu,[29] M. Bellis,[31,5] N. Benmouna,[14] A.S. Biselli,[11] B.E. Bonner,[32] S. Bouchigny,[35,19] S. Boiarinov,[20,35] R. Bradford,[5] D. Branford,[10] W.K. Brooks,[35] S. Bültmann,[29] V.D. Burkert,[35] C. Butuceanu,[39] J.R. Calarco,[26] S.L. Careccia,[29] D.S. Carman,[35] B. Carnahan,[6] A. Cazes,[34] S. Chen,[13] P.L. Cole,[35,16] P. Collins,[2] P. Coltharp,[13] D. Cords,[35,†] P. Corvisiero,[18] D. Crabb,[38] H. Crannell,[6] V. Crede,[13] J.P. Cummings,[31] R. De Masi,[7] R. De Vita,[18] E. De Sanctis,[17] P.V. Degtyarenko,[35] H. Denizli,[30] L. Dennis,[13] A. Deur,[35] C. Djalali,[34] G.E. Dodge,[29] J. Donnelly,[15] D. Doughty,[8,35] P. Dragovitsch,[13] M. Dugger,[2] K.V. Dharmawardane,[29,‡] S. Dytman,[30] O.P. Dzyubak,[34] H. Egiyan,[39,35,§] K.S. Egiyan,[40,†] L. Elouadrhiri,[8,35] P. Eugenio,[13] R. Fatemi,[38] G. Fedotov,[25] R.J. Feuerbach,[5] T.A. Forest,[29] A. Fradi,[19] H. Funsten,[39] M. Garçon,[7] G. Gavalian,[26,29] G.P. Gilfoyle,[33] K.L. Giovanetti,[21] F.X. Girod,[7] J.T. Goetz,[3] E. Golovatch,[18,¶] R.W. Gothe,[34] K.A. Griffioen,[39] M. Guidal,[19] M. Guillo,[34] N. Guler,[29] L. Guo,[35] V. Gyurjyan,[35] C. Hadjidakis,[19] K. Hafidi,[1] R.S. Hakobyan,[6] J. Hardie,[8,35] D. Heddle,[8,35] F.W. Hersman,[26] K. Hicks,[28] I. Hleiqawi,[28] M. Holtrop,[26] M. Huertas,[34] C.E. Hyde-Wright,[29] Y. Ilieva,[14] D.G. Ireland,[15] B.S. Ishkhanov,[25] E.L. Isupov,[25] M.M. Ito,[35] D. Jenkins,[37] H.S. Jo,[19] K. Joo,[9] H.G. Juengst,[29] N. Kalantarians,[29] C. Keith,[35] J.D. Kellie,[15] M. Khandaker,[27] K.Y. Kim,[30] K. Kim,[22] W. Kim,[22] A. Klein,[29,**] F.J. Klein,[12,6] M. Klusman,[31] M. Kossov,[20] L.H. Kramer,[12,35] V. Kubarovsky,[31,35] J. Kuhn,[31,5] S.E. Kuhn,[29] S.V. Kuleshov,[20] J. Lachniet,[5,29] J.M. Laget,[7,35] J. Langheinrich,[34] D. Lawrence,[24] Ji Li,[31] A.C.S. Lima,[14] K. Livingston,[15] H. Lu,[34] K. Lukashin,[6] M. MacCormick,[19] N. Markov,[9] S. McAleer,[13] B. McKinnon,[15] J.W.C. McNabb,[5] B.A. Mecking,[35] M.D. Mestayer,[35] C.A. Meyer,[5] T. Mibe,[28] K. Mikhailov,[20] R. Minehart,[38] M. Mirazita,[17] R. Miskimen,[24] V. Mokeev,[25] L. Morand,[7]

S.A. Morrow,[19,7] M. Moteabbed,[12] J. Mueller,[30] G.S. Mutchler,[32] P. Nadel-Turonski,[14] R. Nasseripour,[12,34] S. Niccolai,[14,19] G. Niculescu,[21] I. Niculescu,[14,21] B.B. Niczyporuk,[35] M.R. Niroula,[29] R.A. Niyazov,[29,35] M. Nozar,[35] G.V. O'Rielly,[14] M. Osipenko,[18,25] A.I. Ostrovidov,[13] K. Park,[22] E. Pasyuk,[2] C. Paterson,[15] S.A. Philips,[14] J. Pierce,[38] N. Pivnyuk,[20] D. Pocanic,[38] O. Pogorelko,[20] E. Polli,[17] S. Pozdniakov,[20] B.M. Preedom,[34] J.W. Price,[4] Y. Prok,[38,††] D. Protopopescu,[26,15] L.M. Qin,[29] B.A. Raue,[12,35] G. Riccardi,[13] G. Ricco,[18] M. Ripani,[18] G. Rosner,[15] P. Rossi,[17] D. Rowntree,[23] P.D. Rubin,[33] F. Sabatié,[29,7] C. Salgado,[27] J.P. Santoro,[37,35,‡‡] V. Sapunenko,[18,35] R.A. Schumacher,[5] V.S. Serov,[20] Y.G. Sharabian,[35] J. Shaw,[24] N.V. Shvedunov,[25] A.V. Skabelin,[23] E.S. Smith,[35] L.C. Smith,[38] D.I. Sober,[6] A. Stavinsky,[20] S.S. Stepanyan,[22] S. Stepanyan,[35,8,40] B.E. Stokes,[13] P. Stoler,[31] S. Strauch,[34] R. Suleiman,[23] M. Taiuti,[18] S. Taylor,[32] D.J. Tedeschi,[34] U. Thoma,[35,§§] A. Tkabladze,[14] S. Tkachenko,[29] L. Todor,[5] M. Ungaro,[9] M.F. Vineyard,[36,33] A.V. Vlassov,[20] L.B. Weinstein,[29] D.P. Weygand,[35] M. Williams,[5] E. Wolin,[35] M.H. Wood,[34,¶¶] A. Yegneswaran,[35] J. Yun,[29] L. Zana,[26] J. Zhang,[29] B. Zhao,[9] and Z. Zhao[34]

(The CLAS Collaboration)

[1]*Argonne National Laboratory, Argonne, Illinois 60439*

[2]*Arizona State University, Tempe, Arizona 85287-1504*

[3]*University of California at Los Angeles, Los Angeles, California 90095-1547*

[4]*California State University, Dominguez Hills, Carson, CA 90747*

[5]*Carnegie Mellon University, Pittsburgh, Pennsylvania 15213*

[6]*Catholic University of America, Washington, D.C. 20064*

[7]*CEA-Saclay, Service de Physique Nucléaire, F91191 Gif-sur-Yvette, France*

[8]*Christopher Newport University, Newport News, Virginia 23606*

[9]*University of Connecticut, Storrs, Connecticut 06269*

[10]*Edinburgh University, Edinburgh EH9 3JZ, United Kingdom*

[11]*Fairfield University, Fairfield, CT 06824*

[12]*Florida International University, Miami, Florida 33199*

[13]*Florida State University, Tallahassee, Florida 32306*

[14]*The George Washington University, Washington, DC 20052*

[15]*University of Glasgow, Glasgow G12 8QQ, United Kingdom*

[16]*Idaho State University, Pocatello, Idaho 83209*

[17]*INFN, Laboratori Nazionali di Frascati, 00044 Frascati, Italy*

[18]*INFN, Sezione di Genova, 16146 Genova, Italy*

[19]*Institut de Physique Nucleaire ORSAY, Orsay, France*

[20]*Institute of Theoretical and Experimental Physics, Moscow, 117259, Russia*

[21]*James Madison University, Harrisonburg, Virginia 22807*

[22]*Kyungpook National University, Daegu 702-701, South Korea*

[23]*Massachusetts Institute of Technology, Cambridge, Massachusetts 02139-4307*

[24]*University of Massachusetts, Amherst, Massachusetts 01003*

[25]*Moscow State University, General Nuclear Physics Institute, 119899 Moscow, Russia*

[26]*University of New Hampshire, Durham, New Hampshire 03824-3568*

[27]*Norfolk State University, Norfolk, Virginia 23504*

[28]*Ohio University, Athens, Ohio 45701*

[29]*Old Dominion University, Norfolk, Virginia 23529*

[30]*University of Pittsburgh, Pittsburgh, Pennsylvania 15260*

[31]*Rensselaer Polytechnic Institute, Troy, New York 12180-3590*

[32]*Rice University, Houston, Texas 77005-1892*

[33]*University of Richmond, Richmond, Virginia 23173*

[34]*University of South Carolina, Columbia, South Carolina 29208*

[35]*Thomas Jefferson National Accelerator Facility, Newport News, Virginia 23606*

[36]*Union College, Schenectady, NY 12308*

[37]*Virginia Polytechnic Institute and State University, Blacksburg, Virginia 24061-0435*

[38]*University of Virginia, Charlottesville, Virginia 22901*

[39]*College of William and Mary, Williamsburg, Virginia 23187-8795*

[40]*Yerevan Physics Institute, 375036 Yerevan, Armenia*

(Dated: December 17, 2007)

Abstract

The ratio of inclusive electron scattering cross sections for ^{15}N/^{12}C was determined in the kinematic range $0.8 < W < 2$ GeV and $0.2 < Q^2 < 1$ GeV^2 using 2.285 GeV electrons and the CLAS detector at Jefferson Lab. The ratio exhibits only slight resonance structure, as predicted by a phenomenological model, and also by quark-hadron duality. Within the super-scaling quasi-elastic model, slight evidence is found for a 1 MeV lower effective nucleon binding energy in ^{15}N than in ^{12}C. Ratios of ^{4}He/^{12}C using 1.6 to 2.5 GeV electrons are in good agreement with the phenomenological model.

PACS numbers: 25.30.Fj,13.60.Hb,27.20.+n

*Electronic address: bosted@jlab.org; Corresponding author.

†Deceased

‡Current address:Thomas Jefferson National Accelerator Facility, Newport News, Virginia 23606

§Current address:University of New Hampshire, Durham, New Hampshire 03824-3568

¶Current address:Moscow State University, General Nuclear Physics Institute, 119899 Moscow, Russia

**Current address: Los Alamos National Laboratory, Los Alamos, New Mexico 87545

††Current address:Massachusetts Institute of Technology, Cambridge, Massachusetts 02139-4307

‡‡Current address:Catholic University of America, Washington, D.C. 20064

§§Current address:Physikalisches Institut der Universität Giessen, 35392 Giessen, Germany

¶¶Current address:University of Massachusetts, Amherst, Massachusetts 01003

I. INTRODUCTION

The ammonia molecules $^{15}NH_3$ and $^{15}ND_3$ are among the most commonly used target media in measurements of the spin structure of the proton and deuteron. In order to correct inclusive electroproduction measurements for the contributions from the only slightly polarized ammonia, it is necessary to know the ratio of cross sections for ^{15}N to the proton or deuteron. Because it is impractical to routinely use a pure ^{15}N target, most experiments make reference measurements with a pure carbon target instead, and use a model to evaluate the $^{15}N/^{12}C$ ratio. Such modeling is relatively reliable in the deep-inelastic region (missing mass $W > 2$ GeV, four momentum transfered $Q^2 > 1$ GeV^2) where one expects the n/p ratio in a nucleus to be very similar to that determined from d/p ratios. The "EMC effect"[1] (difference in the Bjorken x-dependence of the average cross section) is similar, because C and N have similar densities and radii. In the nucleon resonance region ($W < 2$ GeV), the effects of Fermi motion of the nucleons, as well as Meson Exchange Currents (MEC) and Final State Interactions (FSI), are much larger in nuclei than in deuterium, so one can no longer simply use d/p ratios to account for the neutron excess in medium-heavy nuclei such as ^{15}N. In order to constrain these models, it is desirable to confront them with data. Since, to the best of our knowledge, no such measurements existed previously, the Eg1b experiment [2] at Jefferson Lab undertook them in 2001. This article reports on the results obtained with a 2.285 GeV electron beam scattered from carbon and solid nitrogen targets immersed in a liquid-helium bath. To test the model used to correct for the liquid-helium corrections, we also analyzed data at several beam energies with and without the carbon disk present in the liquid helium bath.

II. MEASUREMENTS

The Eg1b experiment measured electron scattering from NH_3, ND_3, C and N targets. This paper reports the results from the C and N targets and from the liquid He in the target vessel. The incident electron energy ranged from 1.7 to 5 GeV and the beam currents ranged from 1 to 5 nA. The beam diameter was less than 1 mm, so to avoid melting the nitrogen, deflecting magnets were used to uniformly raster the beam over the face of the target. Electrons scattered at angles between 10 and 45 degrees were detected in CLAS [3].

In order to minimize the effects of slow drifts in detector response and beam properties, data collection was switched between the ^{12}C and ^{15}N targets every few hours over the course of the 1.5-day-long data taking period for the beam energy of 2.285 GeV.

Data were taken periodically during the main production part of the experiment (focusing on polarized NH_3 and ND_3 targets) with carbon and "empty" targets, both immersed in a liquid-helium bath. This allowed the extraction of the ratio of He/C cross sections with very high statistical precision for beam energies of 1.603, 1.721 and 2.285 GeV.

III. TARGET PROPERTIES

The polarized target for Eg1b utilized a 5 T magnetic field and was cooled with liquid helium to 1 K [4]. An overall view is shown in Fig. 1. To obtain the high vacuum needed to maintain this low temperature, there were several thin windows in the target can, whose total thickness was of order 0.1% radiation lengths. The targets for the experiment were inserted vertically in a tube, referred to as the "banjo". Only one target at a time could be inserted into the beam line. The vertex resolution was not good enough to separate the banjo windows (about 2.3 cm apart) from the other materials in the target, so the vertex cut was made wide enough to include them. The banjo windows were made of 0.071-mm-thick aluminum. Between the two banjo windows was a "mini-cup" containing liquid helium and the target cups. The windows for this mini-cup were about 1.7 cm apart, and were made from 0.127-mm-thick Kapton. The carbon target was a 1.5-cm-diameter disk with density of 2.21 gm/cm^2 and length 0.227 cm. It was mounted in a target cup with a 0.050-mm-thick Kapton foil on one end, and a 0.071-mm-thick aluminum foil on the other end. It was immersed in liquid ^{4}He at 1 K for most of the running. The density of liquid ^{4}He was assumed to be 0.145 gm/cm^3, and the effective length was between 1.7 and 2.3 cm. The ambiguity comes about because it was not possible to unambiguously ascertain if the helium overflowed the mini-cup to fill the two 0.3 cm gaps between the mini-cup and the banjo windows or not. Based on a single short data taking "run" in which the helium was being drained from the target, it appears probable that the helium was not overflowing the mini-cup, so that option was used in the data analysis (with the alternate option included in the systematic error estimate). The nitrogen target consisted of a specially-designed container with two 0.127-mm-thick bowed Kapton windows. The average distance between

the windows was nominally 0.575 cm, with an estimated error of 0.03 cm. Liquid nitrogen (isotopically pure ^{15}N) was poured slowly into the container via a fill tube and frozen by the liquid helium. For the nitrogen density, we used the value of 1.026 gm/cm^2 measured at 21 K [5] for natural nitrogen, and scaled this by 15/14 for ^{15}N. We assumed no significant temperature dependence in going from 21 K to 1 K.

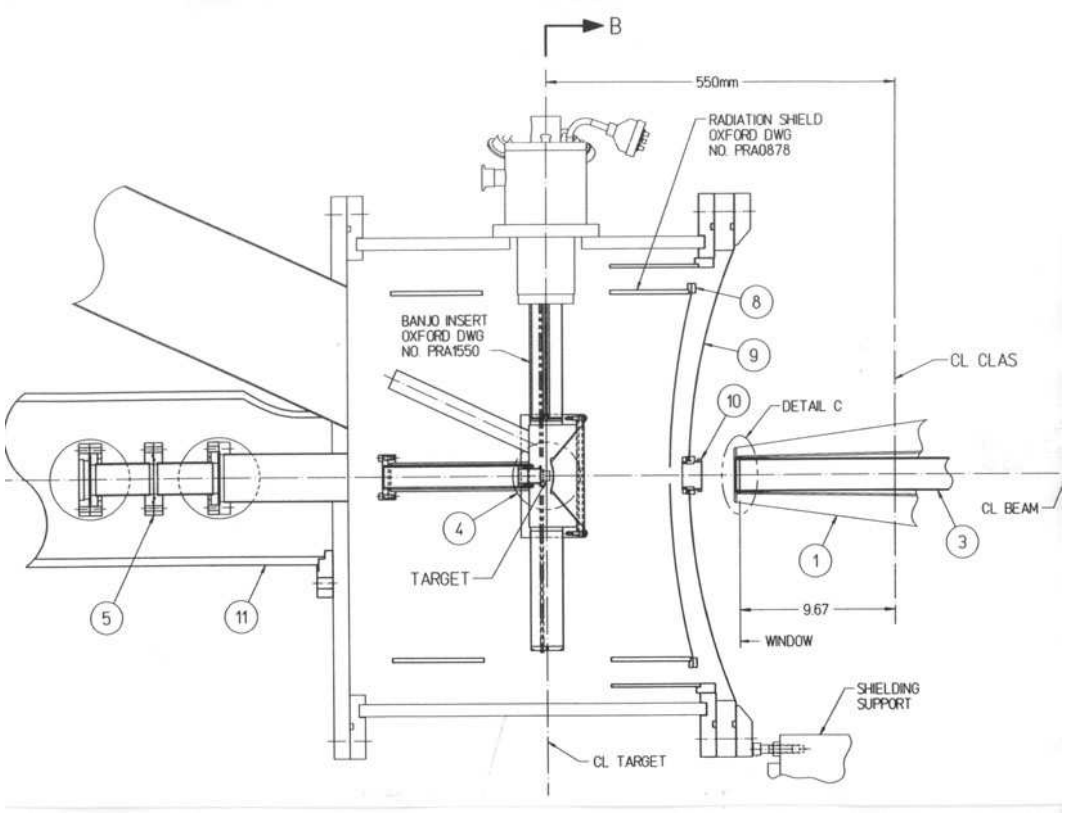

FIG. 1: Overall side view of the polarized target assembly. The beam enters the target chamber from the left through a vacuum window, traverses the liquid-helium filled "banjo" at the center and exits through several thin foils on the right. Various targets can be positioned in the beam by moving a vertical "target stick". The liquid Helium is cooled to about 1 K by a refrigerator (entering diagonally from the upper left). The target region is immersed in a uniform 5 T magnetic field generated by a superconducting Helmholtz-type coil (not shown in the figure).

In order to check that the ^{15}N cell was completely filled, we plot the relative count rate as a function of beam position in the bottom panel of Fig. 2. It can be seen that the target is uniformly filled. We also looked at a data run with the carbon target that was interleaved between two ^{15}N runs (middle plot). Compared to a run taken earlier using the carbon

target on the target stick used for NH_3 production running (top plot), there is a definite indication of some kind of unexpected structure near the top. The feature is independent of azimuthal angle about the beam line, and thus is not due to particular detector problems. Based on the change in the ratio of rates from the top and bottom halves of the targets, we estimate a 2% overall error in the effective carbon target thickness. Note that the vertical and horizontal bands crossing the center of the targets in Fig. 2 are an artifact of the beam deflection magnet readout system and do not reflect any actual changes in target thicknesses.

In order to measure the water contamination in the nitrogen target, we measured the ratio of counts from the nitrogen and carbon targets in the region near $W = M$, where M is the proton mass and W is the invariant mass of the virtual photon plus nucleon. As illustrated in Fig. 3, the ratio looks perfectly smooth in this region, compared to the large narrow elastic peak from free protons observed from NH_3 over ND_3, shown as the crosses in Fig. 3. Due to the absence of the proton elastic peak in the ratio, we conclude that there was much less than 1% water in the nitrogen target.

IV. DATA ANALYSIS

A. Particle Identification

Electrons were principally identified by requiring a minimum pulse height corresponding to 2.5 photoelectrons in the threshold gas Cherenkov counters, in which the momentum threshold for pions was 2.7 GeV (higher than the highest possible momentum the present analysis). This cut keeps about 90% of the electrons, but rejects over 98% of the pions. Timing and geometric cuts between the Cherenkov detector and the time-of-flight scintillator paddles were also used to reduce pion contamination. We also required $E/P > 0.75$, where E is the energy deposited in the electromagnetic calorimeter (corrected for sampling fraction), and P is the momentum determined by the tracking system. This cut retains about 95% of the electrons, while rejecting 80% to 95% of the pions (depending on P). The distribution of Cherenkov detector signals versus E/P is illustrated in Fig. 4, along with the cuts used, for the 2.285 GeV beam energy data set. Combined with the requirement $P > 0.5$ GeV, and π/e ratios as large a 500:1 in some bins, these cuts resulted in at most a few percent pion contamination in the electron sample. The cut value of $P > 0.5$ GeV, which was well

above the trigger threshold of about 0.3 GeV, was chosen to minimize the uncertainties in radiative corrections, pair-symmetric backgrounds, and pion contamination.

A cut on the reconstructed vertex position was used to reject events coming from windows more than 3 cm from the nominal target center. A geometrical cut was used to remove events which could have passed through the photomultiplier tubes of the gas Cherenkov counter (thus causing a false signal). These events can be seen as the bands on the far left side of Fig. 5. This cut was also adjusted to ensure that particles passed through regions of $> 90\%$ Cherenkov counter efficiency, as illustrated in Fig. 5. This was found to be important because the efficiency is primarily a function of the particle trajectory relative to the Cherenkov mirrors. For a particular value of Q^2 and W, the efficiency depends mainly on z, the position of the interaction point along the beam line. The carbon target was centered 3 mm up-stream from the nitrogen target, and is also shorter, which is enough to cause up to 10% differences in Cherenkov efficiency near the edges of the mirrors. Requiring the efficiency to be $> 90\%$ removes essentially all of this bias. An unfortunate consequence is that cross section ratios cannot be determined to as low Q^2 as without this cut.

As in previous analysis of data from this experiment [6], small corrections to the reconstructed particle angles and momenta were made taking into account the beam position for a given event and misalignments of the drift chambers and torus coils. These effects largely cancel in the ratio of the two target rates, but these corrections result in narrower quasi-elastic peaks, which are better centered near the mass of the nucleon.

B. Count ratios

Ratios were formed of count rates from the nitrogen and carbon targets, normalized to the live-time corrected total beam charge incident on each target. The ratios are shown for nine bins in Q^2 as a function of the final state invariant mass W in Fig. 6. The results shown are from one of two independent analyses of the data summary tapes; results from the other analysis were almost identical. The main differences were in the choice of bin sizes, the choice of files meeting quality standards, and the implementation of momentum, angle, and other corrections.

Also shown in Fig. 6 as the solid curves are the predicted ratios (including radiative effects) from the model discussed in more detail below. To obtain the overall best agree-

ment with the data, the thickness of the ^{15}N cell was adjusted upward by $\delta_N = 3.0\%$ from the nominal value. The factor was obtained by minimizing the value of $\chi^2 = \sum_i [r_i^E(W^2,Q^2) - r_i^M(W^2,Q^2)]^2/[\delta r_i^E(W^2,Q^2)]^2$ in the kinematic region $W > 1.2$ GeV, where r_i^E are the experimental cross section ratios obtained using a particular cell length, δr_i^E are the experimental statistical errors, and r_i^M are the model ratios. The cut $W > 1.2$ GeV was chosen to minimize the sensitivity to the exact positions and widths of the carbon and nitrogen quasi-elastic peaks, which are the only narrow structures in the cross sections. This nitrogen cell length adjustment of 3.0% is well within the estimated 6% uncertainty in the cell length, and the correlated 2% uncertainty in the carbon target length. As a guide to the systematic error in δ_N, we changed the W cut to $W > 0.8$ GeV, obtaining $\delta_N = 3.1\%$, and to $W > 1.3$ GeV, obtaining $\delta_N = 2.9\%$. This suggests that the systematic error on δ_N is about 0.1%. The change in the W-dependence of the radiative corrections with changing target lengths was fully taken into account in the χ^2 minimization, which made the procedure non-trivial.

C. Pair-Symmetric and Pion Contamination

Some of the events identified as electrons originate from $\pi^0 \to \gamma\gamma$ decays in which one of the photons converts to an e^+e^- pair either in the field of the pion (Dalitz decay), or in the field of a nucleus in material in or near the target. Since this process is pair-symmetric, the relative rate can be measured by comparing the rates of positrons and electrons taken with opposite torus polarities. While this was not done at the beam energy of 2.285 GeV, it was done with a beam energy of 2.5 GeV for ammonia and carbon targets. The measured ratios are plotted as a function of W for the nine Q^2 bins of this study in Fig. 7. The ratio rises rapidly at low values of scattered electron momentum P (i.e., high values of W), and typically crosses 5% for W values corresponding to $P = 0.5$ GeV (vertical dashed lines in Fig. 7). We used this cut in the data analysis not only to keep the pair-symmetric correction below 5%, but also to keep the radiative corrections from becoming too large.

For the present analysis, what matters is the possible difference in pair-symmetric contamination between the carbon and nitrogen targets. We assume a possible difference of ± 0.001 radiation lengths (r.l.) (they are both nominally about 0.01 r.l. of total material), and assume that photon conversions take place on average in half of the target cup. Taking

into account that, in this situation, about 2/3 of the pair-symmetric events originate from direct Dalitz decays (1.2% of all π^0 decays), and that, on average, 7/9 photons convert per radiation length of material, we estimate an upper limit of less than 5% in the relative difference in e^+e^- yields. A larger variation could arise from the A-dependence of neutral pion photoproduction. At very forward angles, this cross section per nucleus could scale with Z or A (coherent production), which would give up to a 25% difference in the yields per nucleon for the two targets. At larger angles, where photon shadowing effects are important [7], the per nucleon yields could actually decrease with A (for example as $A^{0.6}/A$), which would produce a 14% difference in the other direction. Since these are quite extreme variations, we reasonably estimate 1 σ systematic errors in the relative pair-symmetric yields between the two targets as 10%. At the highest values of W, where the pair-symmetric ratios are near 5%, this leads to absolute systematic errors as large as 0.5% in the extracted $^{15}\mathrm{N}/^{12}\mathrm{C}$ ratios, quickly becoming negligible at lower values of W.

A related background arises from charged pions misidentified as electrons or positrons. From a study of the Cherenkov response to pions and electrons, we find that less than 2% of particles passing the cuts used to identify positrons are actually pions. Since the possible A-dependence for charged pion production has a smaller range than for π^0 production, and is expected to be similar for π^+ and π^- (as it is only the A-dependence of the π^+ to π^- ratio that matters), the systematic error from pion contamination is much smaller than for the pair-symmetric leptons, and has been subsumed into that correction.

D. Prescription for Radiative Corrections

A correction was made to the data to account for electromagnetic radiative effects, using the standard formalism of Mo and Tsai [8]. These corrections account for "internal" and "external" radiation of photons in the field of a given nucleus. The "internal" radiation takes place on the same nucleus from which the electron scattered, and largely cancels in the ratio of cross sections from different nuclei with similar atomic number. The "external" radiation takes place from nuclei either before or after the interaction vertex, and is proportional to the total thickness (in radiation lengths) of each target. Since each target had a different total thickness, this leads to differences in the predicted ratio of Born-level cross sections and radiated (measured) cross sections, especially for the He/C ratios (since the

He target is substantially thinner in radiation lengths than the C target). Additional differences in radiative corrections for different nuclei come about due to the different W- and Q^2-dependencies of the cross sections for the different nuclear species. Since nuclear elastic tails are generally small for the kinematics of the present experiment, and the quasi-elastic and inelastic cross sections are quite similar for He, C, N, and Al, the radiative correction factors σ_B/σ_R (ratio of Born to radiated cross sections) turn out to be fairly similar for each target employed in this work.

E. Cross Section Models for Radiative Corrections

To quantify these effects, we calculated σ_B and σ_R for each target material (He, C, N, Al), and formed a net radiation correction factor from the sums of the cross sections for each material, weighted by their relative abundance in the corresponding target. The calculations used the nuclear charge radii of Ref. [9] for the elastic form factors (evaluated in the shell model), and the super-scaling model of Ref. [10] for the quasi-elastic cross sections with the nucleon elastic form factor parameterization of Ref. [11]. We assumed values of the effective average binding energy parameters E_s in this model of 15, 20, 20, and 18 MeV for He, C, N, and Al, respectively, and corresponding values of 180, 225, 225, and 236 MeV for the effective Fermi width parameter K_F. We used a polynomial fit to the $F(y)$ scaling function from Ref. [12]. This function was fit to longitudinal cross sections. For lack of a better choice, we used the same function for the transverse cross sections, realizing that meson exchange currents and final state interactions will result in an imperfect description of the quasi-elastic region. These effects are minimized in the ratio of similar nuclei such as C and N. A Pauli-suppression correction at low Q^2 was made using the prescription of Mo and Tsai [8].

Inelastic scattering was modeled using a Fermi-convolution method of "smearing" free proton [13] and neutron [14] cross sections. The neutron cross sections were obtained from a global fit to all available data for inclusive electron scattering from the deuteron, including recently published data from CLAS [15]. The "smearing" was done by simplifying the full four-dimensional integration over a spectral function in missing energy and momentum with a simple one-dimensional step-function integration over the component of Fermi momentum parallel to the virtual photon, using a simple symmetric y-scaling model. The form of the

inelastic cross section used for each target A was given by

$$\sigma_A(W, Q^2) = \sum_{i=1}^{15} [Z\sigma_p(W_i', Q^2) + N\sigma_n(W_i', Q^2)]F_i,$$

where i is the bin number, Z and N are the number of protons and neutrons in the particular nucleus, σ_p and σ_n are the inelastic cross sections for a free proton and neutron,, respectively,

$$(W_i')^2 = W^2 + \eta_i k_F |\vec{q}| - 2E_s(\nu + M),$$

where we have used the same values for k_F and E_s as for the quasi-elastic model for each nucleus, and ν and $\vec{q}$ are the energy and three-momentum transfer, respectively. The fifteen values of the Fermi-smearing parameters η_i are: -3.000, -2.571, -2.143, -1.714, -1.286, -0.857, -0.429, 0.0, 0.429, 0.857, 1.286, 1.714, 2.143, 2.571, and 3.000, for $i = 1$ to 15, respectively. The fifteen values of F_i, determined from a y-scaling function [12] are: 0.0019, 0.0063, 0.0172, 0.0394, 0.0749, 0.1186, 0.1562, 0.1712, 0.1562, 0.1186, 0.0749, 0.0394, 0.0172, 0.0063, and 0.0019. These sum to unity, implying no net nuclear dependence to the Fermi smearing. Instead, an additional overall factor for the A-dependence (the so-called "EMC effect") was modeled using a fit to SLAC data [1]. The assumption was made that the EMC effect is independent of Q^2, depending only on Bjorken x. The correction factor was "frozen" at the value of $x = 0.7$ for values of $x > 0.7$.

F. Effect of Radiative Corrections

In this analysis, we wish to extract $^{15}\mathrm{N}/^{12}\mathrm{C}$ cross section ratios from measured count rate ratios. The kinematic dependence of the scale factors that accounts for the extra helium and target walls is shown as the dashed curves in Fig. 8. These curves are based on the model of Born-level cross sections and the relative abundance of each material. The effect of radiative corrections to the model cross sections is to slightly accentuate the W-dependence of these scale factors, as illustrated by the solid curves in Fig. 8. The largest differences are at low Q^2 and high W, and arise principally due to the difference in nuclear elastic tails. These scale factors were determined using the Born and radiated cross sections for each isotope combined with their assumed abundances in each of the targets. Since radiative corrections are a second-order effect, there is relatively little sensitivity to the models. As seen below, since the C/N and He/C ratios for the quasi-elastic and inelastic models we used agree with

data within a few percent, the systematic error from these models is less than a few tenths of a percent.

G. Systematic Error due to Target Model

In order to evaluate the systematic errors due to target modeling, the entire analysis was repeated seven times, each time changing one of the following items:

- Carbon thickness increased by 2%;
- Carbon thickness decreased by 2%;'
- Liquid helium cell length changed from 1.7 cm to 2.3 cm;
- Kapton foil in carbon target changed from 0.043 to 0.060 gm/cm^2;
- Aluminum foil thickness in the nitrogen target changed from 0.038 to 0.060 gm/cm^2;
- Kapton foil in nitrogen target changed from 0.072 to 0.105 gm/cm^2.

For each analysis, the nitrogen target cell length was adjusted to give the best overall agreement with the model cross sections used for the radiative corrections, as described above. The length adjustment scale factors ranged from 0.99 to 1.04. The average value of the absolute difference in the final N/C cross sections ratios was used as an estimate of the point-to-point systematic variations due to uncertainties in target modeling. The results are small, typically 0.1%, and show relative little variation with kinematics. These errors were added in quadrature with the $< 0.5\%$ errors due to pair-symmetric backgrounds (see above) to give the final point-to-point systematic errors. Note that these are estimates intended to give the order-of-magnitude of possible systematic biases in the results as the errors are highly correlated locally.

V. RESULTS FOR ^{15}N/^{12}C

The final results for the ratio of Born cross section per nucleon for ^{15}N/^{12}C are plotted in Fig. 9 as a function of invariant mass W for nine bins in Q^2 and a beam energy of 2.285 GeV. Numerical results are available from the CLAS data base [16]. Due to the uncertainties in

the target thicknesses, there is an overall normalization error of about 6%, if no a priori knowledge of the expected results is assumed. Assuming that the physics model used for radiative corrections is on average correct in the region $W > 1.2$ GeV, the normalization error is reduced to approximately 0.1%, as discussed above. Additional kinematic-dependent systematic errors are relatively small, and only visible on the plot at the largest values of W. Since the nitrogen cell length was adjusted to give the best overall agreement with the simple model cross section ratios (as described above), the interest in the present results is in the relative kinematic dependence of the ratios.

Five main conclusions are evident from the data:

- Overall, the simple models used for radiative corrections (see above) give a good description of the data.

- The pronounced dips in the ratios near the quasi-elastic peak decrease in depth with increasing Q^2, as expected due the increasing contributions of inelastic scattering, and the increasing ratio of neutron to proton elastic form factors.

- The ratios in the resonance region ($W > 1.1$ GeV) show only slight resonant structure. At lower Q^2, both data and the model show enhanced ratios near the $\Delta(1232)$ peak, where the neutron to proton ratio is expected to be unity due to the isovector nature of this resonance. A slight dip near the $S_{11}(1535)$ resonance is possibly evident. At higher Q^2, corresponding to large three momentum transfer $\vec{q}$, Fermi-smearing effects become larger (since $(W')^2 - W^2$ in leading order is proportional to $\vec{q}$), and the small indications of resonant structure disappear.

- On average, the ratios tend to decrease with increasing Q^2 at fixed W, corresponding to larger values of the Bjorken scaling variable x. In deep-inelastic scattering, σ_n/σ_p is approximately given by $(1 - 0.8x)$ [17]. To approximately take into account target-mass effects, we replaced x with the Nachtmann [18] scaling variable $\xi \equiv 2x/(1 + \sqrt{1 + 4M^2x^2/Q^2})$. The dashed curve generated defined by $^{15}\mathrm{N}/^{12}\mathrm{C}= 1 - (1 - \sigma_n/\sigma_p)/15(1 + \sigma_n/\sigma_p)$ using $\sigma_n/\sigma_p = (1 - 0.8\xi)$, shown in Fig. 9, is a remarkably good approximation of the data, especially at the low Q^2 values of this experiment, where additional higher twist effects might be expected to play a role. This is particularly true if one were to average over the quasi-elastic and Δ

resonance regions [19]. This appears to be yet another manifestation of quark-hadron duality [20, 21].

- There are indications that the ratios are higher than the model predictions in the region between the quasi-elastic peak (W = 0.94 GeV) and the $\Delta(1232)$ resonance (W = 1.22 GeV), particularly in the lower Q^2 bins. This may well be due to the influence of final state interactions and meson exchange currents [22]. It is also possible to reproduce most of the difference with a reduction of 1 MeV in the effective binding energy parameter E_s for ^{15}N, from 20 MeV to 19 MeV, as shown by the dotted curves in Fig. 9. We found that keeping E_s fixed at 20 MeV and varying k_F always made the agreement with data worse. It is possible that simultaneously varying for E_s and k_F could result in slightly better agreement, but this is beyond the scope of the present work. In any case, it is clear that it is easier to describe the data with a simple model in the region $W > 1.2$ GeV (χ^2/d.f.=1.8) than in the quasi-elastic and pion threshold region ($W < 1.2$ GeV), where χ^2/d.f.=6.8. This is an indication that more sophisticated models that include meson-exchange currents and final-state interactions are needed. The present data can provide valuable constraints on such models.

VI. RESULTS FOR ^{4}HE/^{12}C

In order to test the model used in the N/C extraction for radiative corrections and the contributions from He and Al, we analyzed the data taken periodically during the production part of the experiment with "empty" and carbon targets. The "empty" targets had the same windows as the carbon target, but lacked the actual carbon disk. Most of the material in the "empty" target is liquid helium. Using the data with beam energy $E > 5$ GeV, where the ratios of cross sections are very well known in the Deep Inelastic Scattering (DIS) region, we determined the effective length between the mini-cup windows to be 1.8 ± 0.1 cm.

The rates versus beam position were studied to define good runs with no extra material in the empty cell. The study revealed that for the last third of the experiment (data with beam energies of 2.5 and 4.2 GeV), some extra material appeared in the empty cell (possibly while making a repair for a ruptured ND_3 cell window), resulting in a higher count rate than expected from the bottom of the cell, so these data were not used. For the beam energies of

1.6 to 2.2 GeV, we found that the count rate ratios for the empty to carbon targets ($R^{DATA}_{Mt/C}$) were in very good agreement with the predictions of the radiated model ($R^{RADMODEL}_{Mt/C}$) discussed above. For each of the nine Q^2 bins, we determined the beam-energy averaged ratio $r(Q^2, W) = < R^{DATA}_{Mt/C} / R^{RADMODEL}_{Mt/C} >$ as a function of W. To correct for the differences in the radiative corrections, and assuming that the model correctly describes the relatively small contributions from the target windows, we determined the ratio of Born-level cross sections for He/C, shown as the solid circles in Fig. 10, by multiplying the ratio of model Born cross sections by $r(Q^2, W)$. Numerical results are available from the CLAS data base [16]. It can be seen that the results are generally in good agreement with the Born cross section ratio used in the model (solid curves). At moderate Q^2, the present ratios are reasonably consistent with previous data taken at a scattering angle of 37 degrees and beam energies of 0.9 to 1.2 GeV at SLAC [23] (open circles), although these ratios tend to be higher than our results.

VII. SUMMARY

We find that the ratios of electroproduction cross sections for ^{15}N/^{12}C and ^{4}He/^{12}C can be remarkably well described by a simple model based on super-scaling in the quasi-elastic region, and simple y-scaling in the nucleon resonance region, even at Q^2 values as low as 0.1 GeV^2. Little resonance structure is seen in the ratios, except for small effects in the $\Delta(1232)$ region.

VIII. ACKNOWLEDGMENTS

We would like to acknowledge the outstanding efforts of the Accelerator, Target Group, and Physics Division staff that made this experiment possible. This work was supported by the U.S. Department of Energy, the Italian Istituto Nazionale di Fisica Nucleare, the U.S. National Science Foundation, the French Commissariat à l'Energie Atomique and the Korean Engineering and Science Foundation. The Southeastern Universities Research Association (SURA) operated the Thomas Jefferson National Accelerator Facility for the United States

Department of Energy under contract DE-AC05-84ER40150.

---

[1] J. Gomez *et al.*, Phys. Rev. D49, 4348 (1994).

[2] CLAS Collaboration, K.V. Dharmawardane *et al.*, Phys. Lett. B641, 11 (2006); CLAS Collaboration, P.E. Bosted *et al.*, Phys. Rev. C75, 035203 (2007).

[3] B.A. Mecking, *et al.*, Nucl. Instr. Meth., **A503**, 513 (2003).

[4] C.D. Keith *et al.,* Nucl. Instr. Meth. **A501**, 327 (2003).

[5] URL: www.sunysccc.edu/academic/mst/ptable/n.html

[6] K.V. Dharmawardane, Ph.D Thesis, Old Dominion University, 2004 (unpublished); Y. Prok, Ph.D Thesis, University of Virginia, 2004 (unpublished).

[7] D.O. Caldwell *et al.,* Phys. Rev. Lett. 23, 1256 (1969).

[8] L. Mo and Y.-S. Tsai, Rev. Mod. Phys. 41, 205 (1969).

[9] H. de Vries, Atomic Data and Nuclear Data Tables 36, 495 (1987).

[10] T.W. Donnelly and I. Sick, Phys. Rev. Lett. 82, 3212 (1999).

[11] P. Bosted, Phys. Rev. C 51, 409 (1995).

[12] J.E. Amaro *et al.,* Phys. Rev. C71, 015501 (2005).

[13] M.E. Christy, private communication for fit to data in: E94-110 Collaboration, Y. Liang *et al.,* nucl-ex/0410027, JLAB-PHY-04-45, submitted to Phys. Rev. Lett.

[14] P.E. Bosted and M.E. Christy, arXiv:0711.0159 (2007).

[15] CLAS Collaboration, M. Osipenko *et al.,* Phys. Rev. C73, 045205 (2006).

[16] URL: clasweb.jlab.org/physicsdb/

[17] B. Adeva *et al.* Phys. Rev. D 58, 112001 (1998).

[18] O. Nachtmann, Nucl. Phys. **63**, 237 (1975).

[19] F.E. Close and N. Isgur, Phys. Lett. **B509**, 81 (2001); F.E. Close and W. Melnitchouk, Phys. Rev. C **68**, 035210 (2003).

[20] W. Melnitchouk, R. Ent, C. Keppel, Phys. Rep. **406**, 127 (2005).

[21] CLAS Collaboration, P.E. Bosted *et al.*, Phys. Rev. C75, 035203 (2007).

[22] J.E. Amaro, M.B. Barbaro, T.W. Donnelly, and A. Molinari, Phys. Rept. 368, 317 (2002).

[23] R.M. Sealock *et al.,* Phys. Rev. Lett. 62, 1350 (1989).

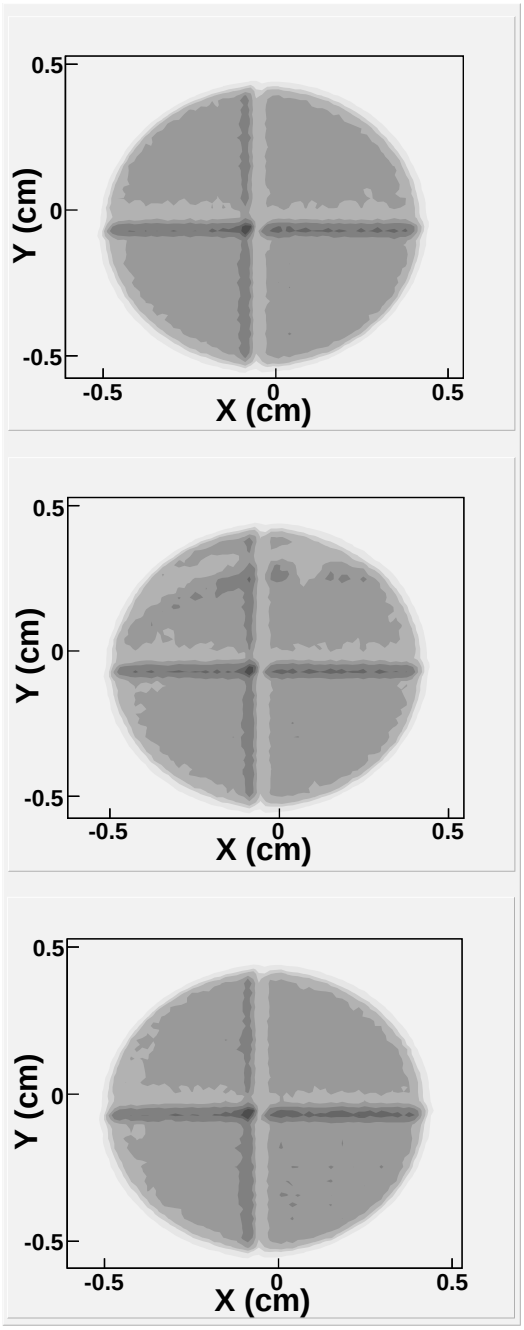

FIG. 2: Relative count rate over the front face of targets. *Top*: carbon target from the polarized ammonia stick, used just before the carbon/nitrogen comparisons. *Middle*: carbon target interleaved between two nitrogen target runs. *Bottom*: Typical ^{15}N target. The "cross hair" features are an artifact of the magnet readout system.

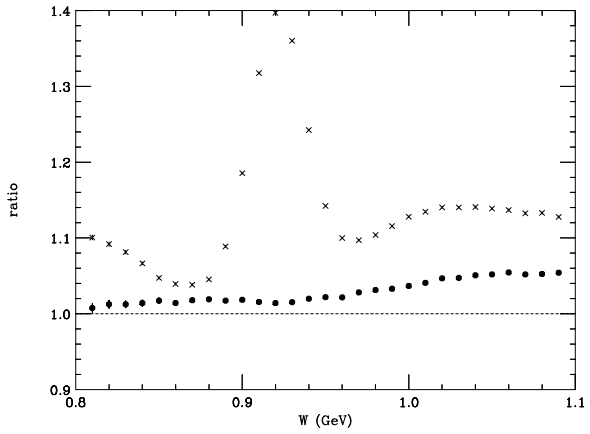

FIG. 3: Ratio of counts from nitrogen to carbon in the region of the free proton elastic peak (solid circles). The ratio from NH_3 to ND_3 is shown as the crosses, where a free proton elastic peak is clearly visible.

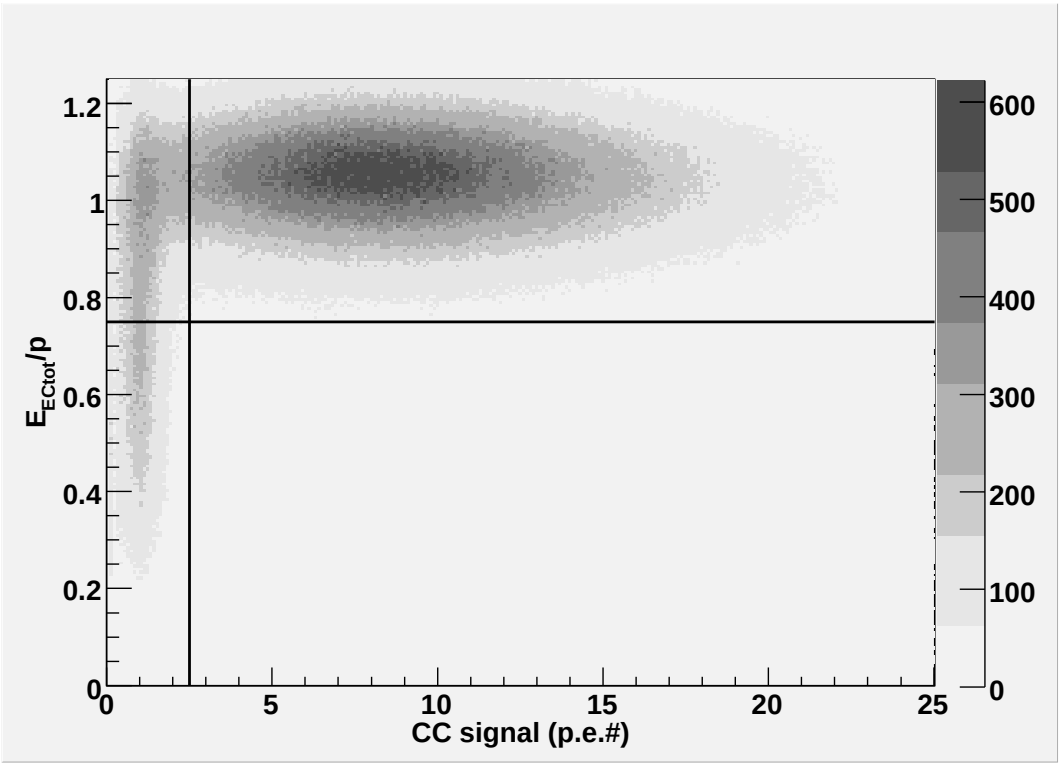

FIG. 4: The distribution of gas Cherenkov detectors signals (in units of photoelectrons) versus E/P (the ratio of sampling fraction corrected calorimeter energy divided by tracked particle momentum) for the 2.285 GeV beam energy data set. The lines indicate the cuts used to identify electrons.

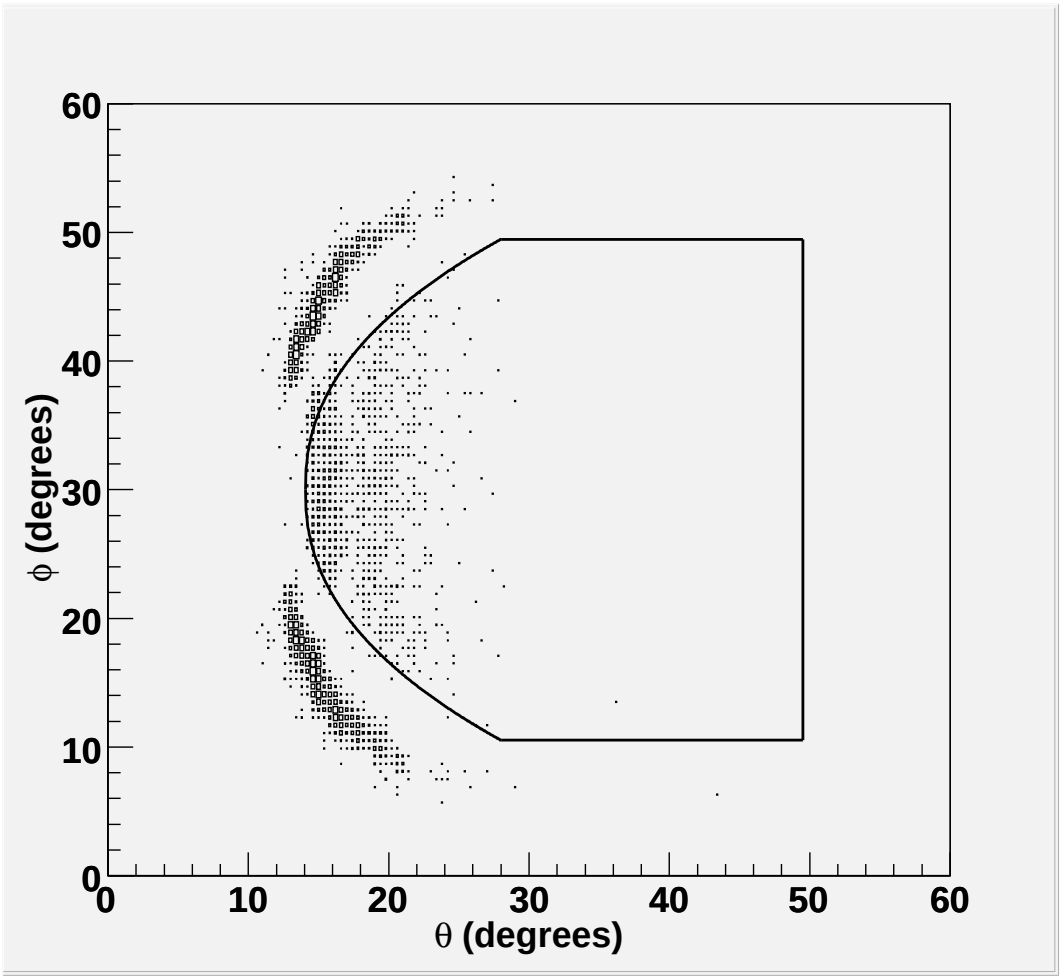

FIG. 5: The distribution of events producing a significant gas Cherenkov detector signal as a function of polar and azimuthal angles in one of the sectors of CLAS. The curve illustrates the geometrical cut used to remove events that hit the photo-cathodes of the detector photo-multipliers (bands on left side of plot).

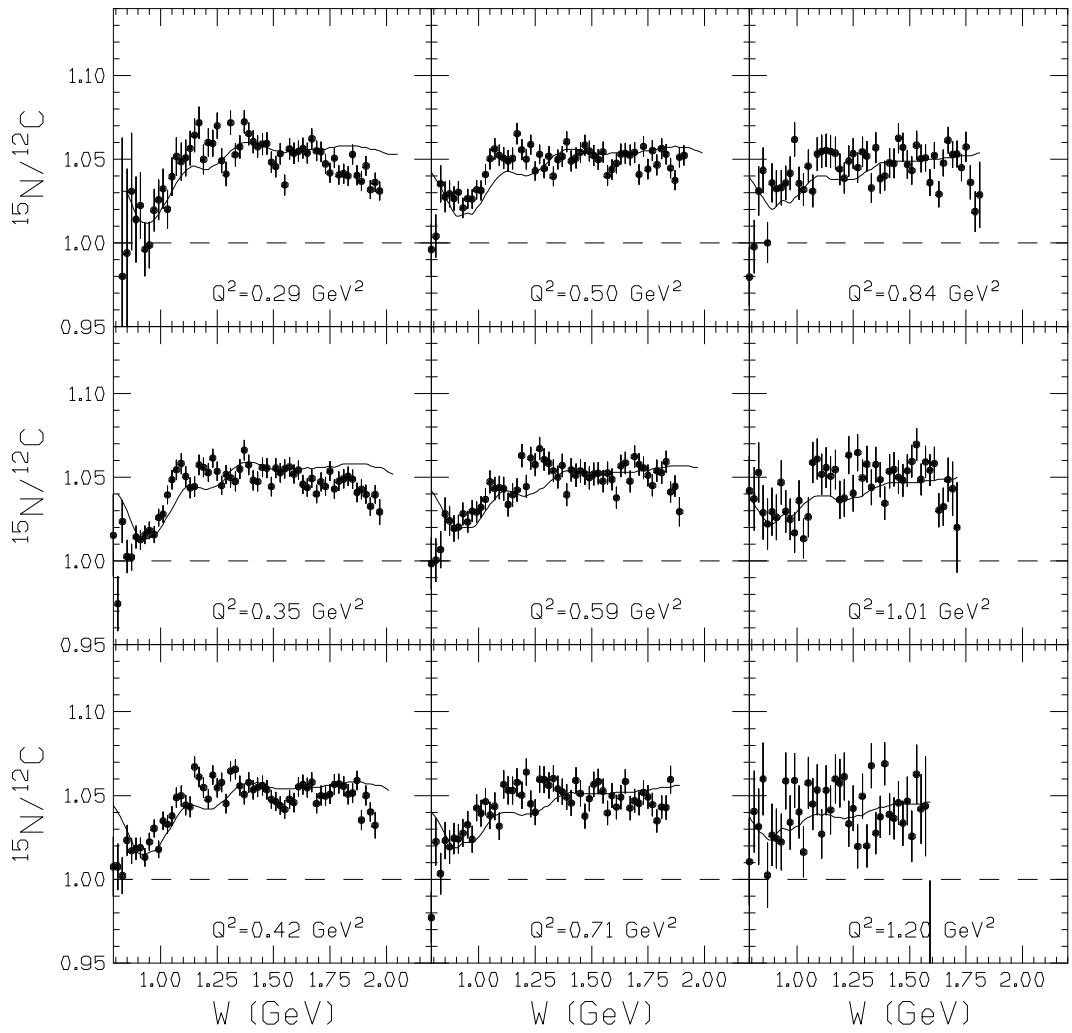

FIG. 6: Ratios of count rates from the nitrogen and carbon targets as a function of missing invariant mass W, for 9 bins in Q^2 (in units of GeV^2). The rates have been normalized to the number of incident electrons and corrected for detector live-time. The curves are the predictions of the model including radiative effects, with the length of the nitrogen cell adjusted to give the best overall agreement with the data.

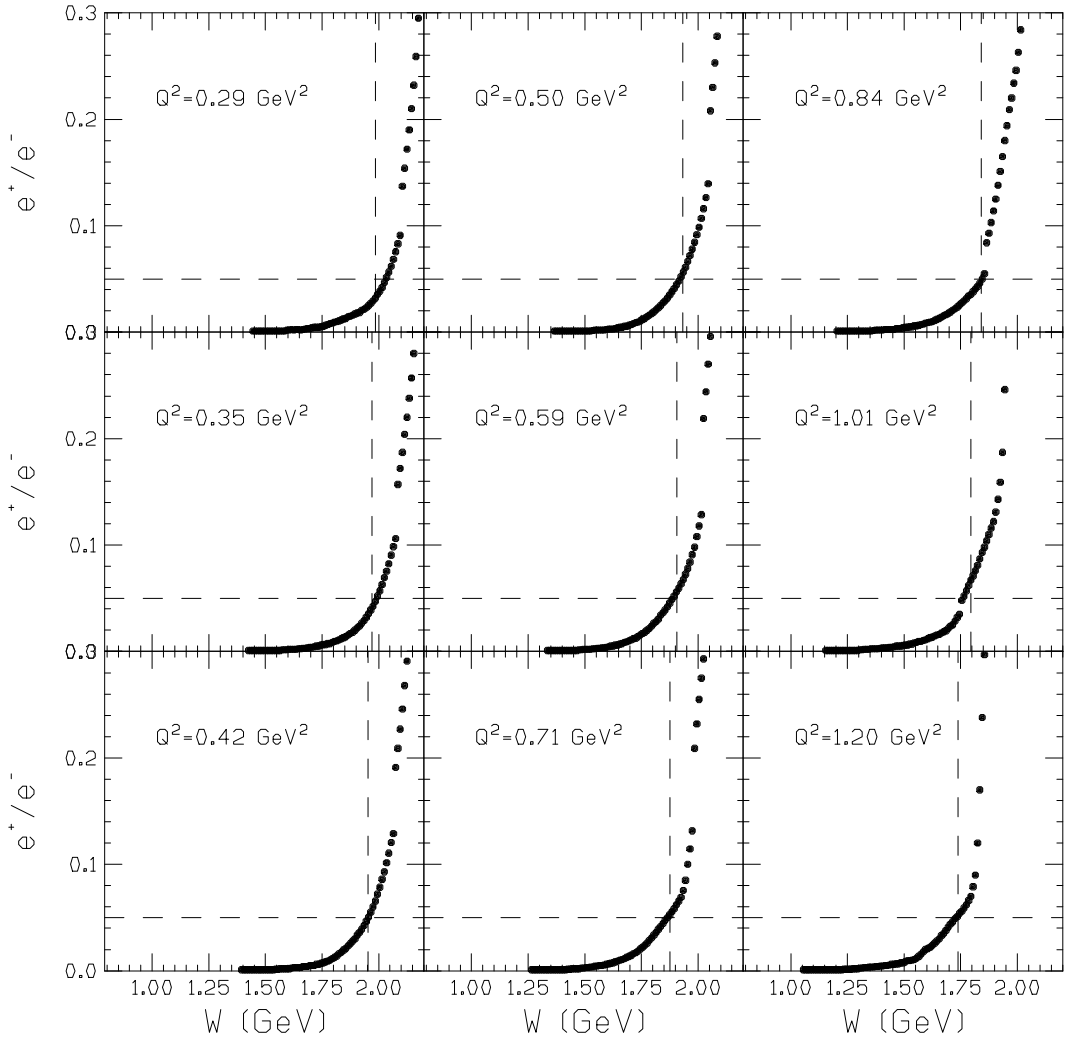

FIG. 7: Ratio of positrons to electrons as a function of W for the Q^2 bins of this analysis. The vertical dashed lines correspond to the cut used.

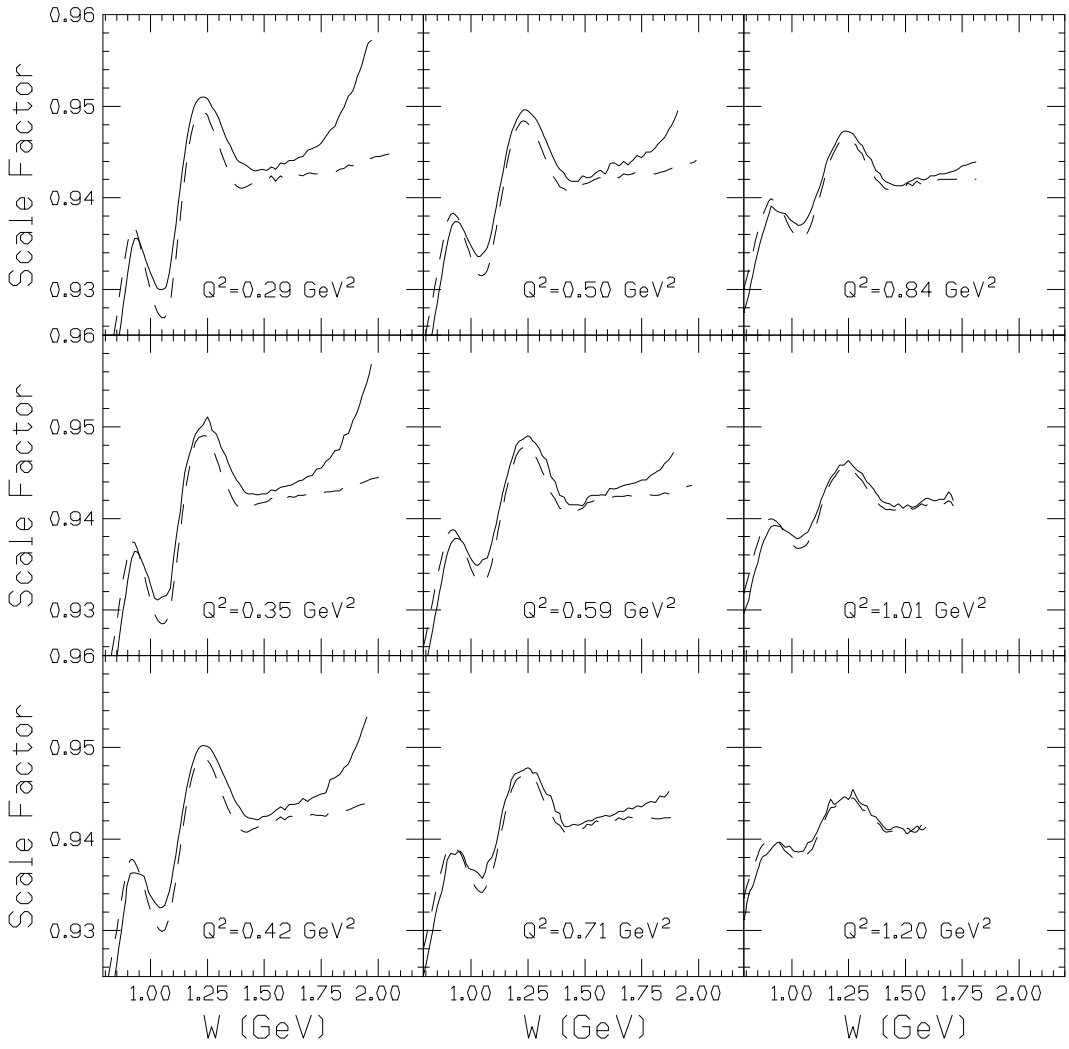

FIG. 8: The curves show the multiplicative scale factors to convert measured count ratios for the nitrogen divided by the carbon targets, to the cross section ratios per nucleon for pure ^{15}N and ^{12}C isotopes. The solid curves include the effects of different radiative corrections for the two targets, while the dashed curves are what would be obtained if the radiative corrections were identical for each target.

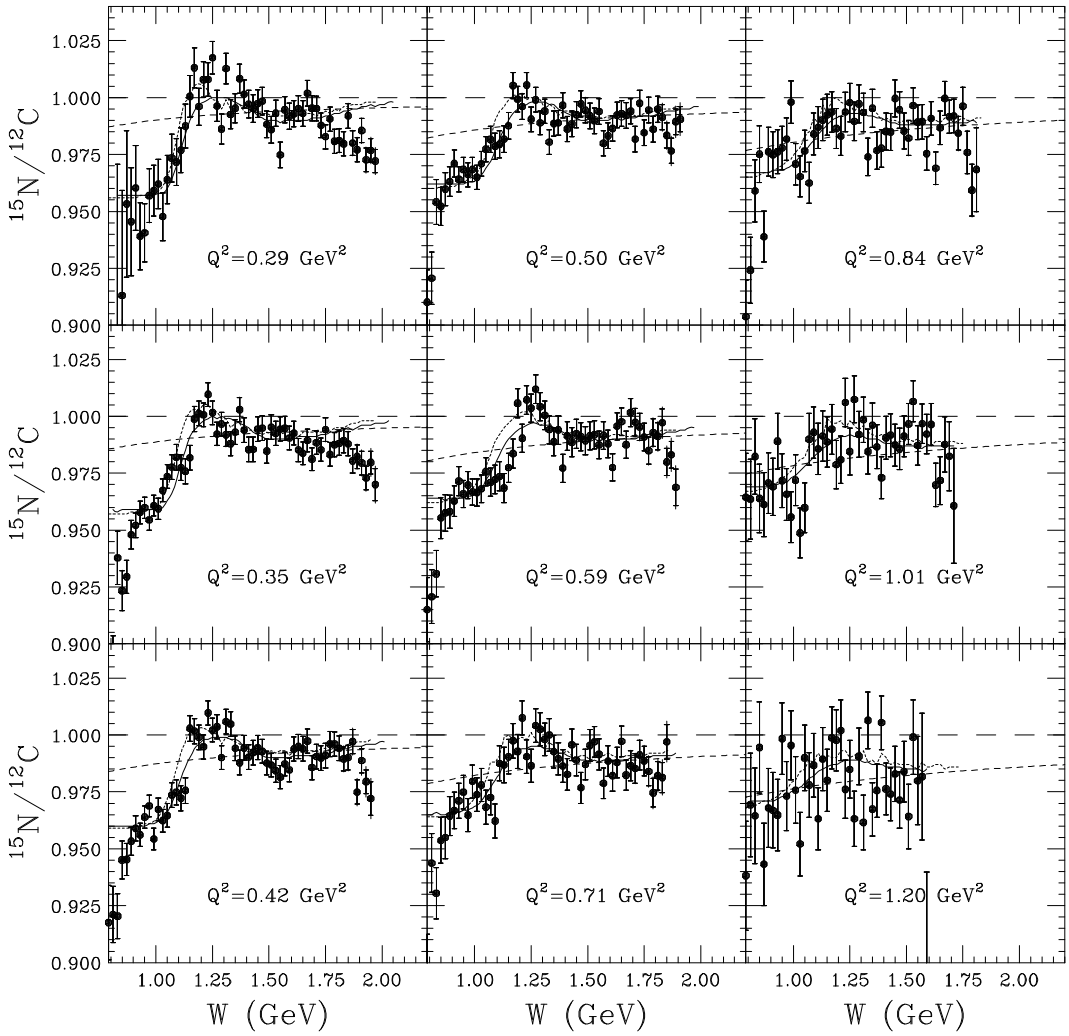

FIG. 9: Extracted ratios of cross sections per nucleon for pure ^{15}N to ^{12}C from this experiment. The inner errors are statistical only, while the outer bars include point-to-point systematic errors added in quadrature. There is a large overall normalization error of 6%. The solid curves shows the ratio of model cross sections with $E_s = 20$ MeV for both C and N, while dotted curve used 19 MeV for N. The dashed curves were generated using $\sigma_n/\sigma_p = (1 - 0.8\xi)$. The long dashed lines are plotted at unity, for reference.

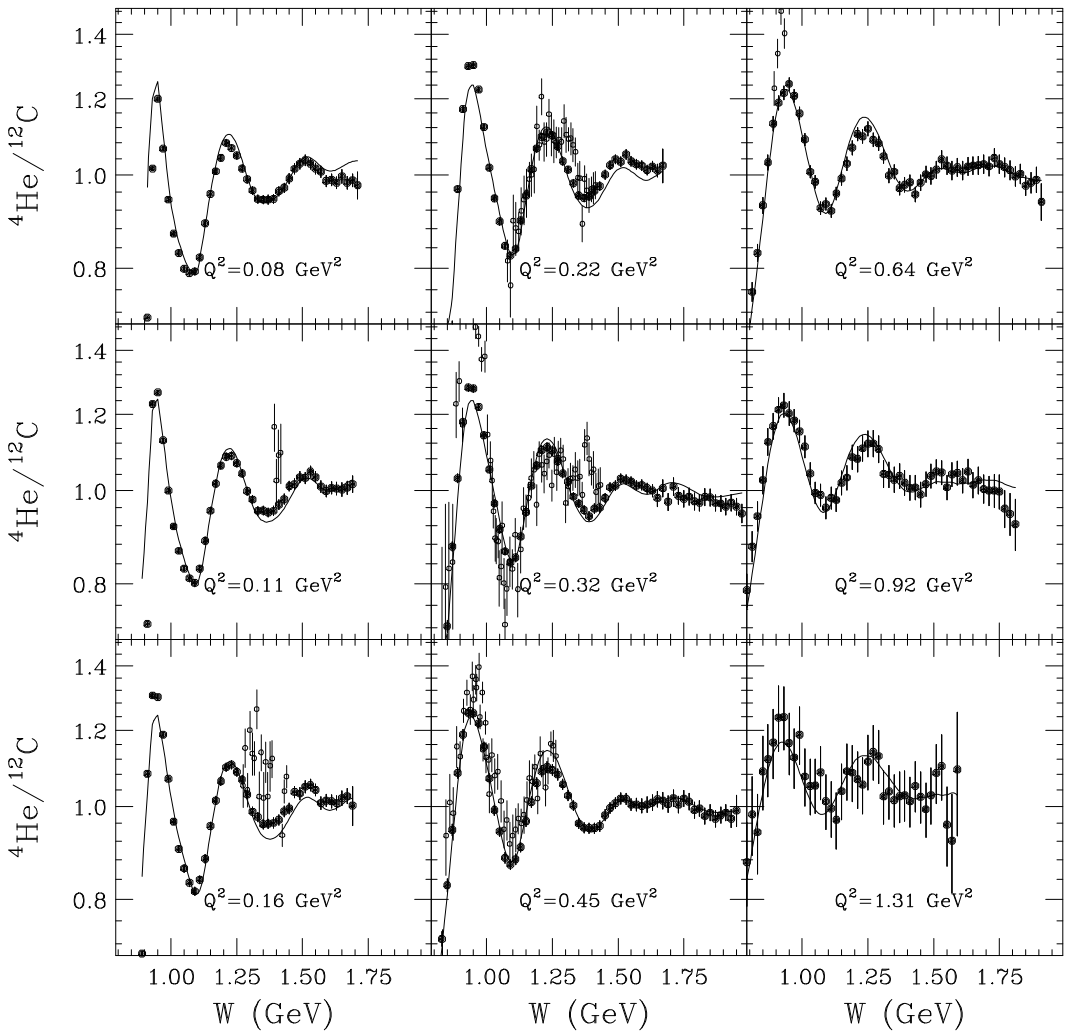

FIG. 10: Extracted ratios of ^{4}He to ^{12}C from this experiment (solid circles), using beam energies of 1.6 to 2.2 GeV. The errors are statistical only. The overall normalization error is about 4%. The solid curves show the ratio of model cross sections. The open circles are from SLAC experiment NE5 [23].